Fast and dense magneto-optical traps for strontium

S. Snigirev,[1] A. J. Park,[1] A. Heinz,[1] I. Bloch,[1,2] and S. Blatt[1,*]

[1]*Max-Planck-Institut für Quantenoptik, Hans-Kopfermann-Straße 1, 85748 Garching, Germany*

[2]*Fakultät für Physik, Ludwig-Maximilians-Universität München, 80799 München, Germany*

(Received 20 March 2019; published 20 June 2019)

We improve the efficiency of sawtooth-wave adiabatic-passage cooling for strontium atoms in three dimensions and combine it with standard narrow-line laser cooling. With this technique, we create strontium magneto-optical traps with 6×10^7 bosonic ^{88}Sr (1×10^7 fermionic ^{87}Sr) atoms at phase-space densities of 2×10^{-3} (1.4×10^{-4}). Our method is simple to implement and is faster and more robust than traditional cooling methods.

DOI: 10.1103/PhysRevA.99.063421

I. INTRODUCTION

Ultracold strontium (Sr) atoms are used in optical frequency standards [1], in superradiant lasers [2] and atom interferometers [3], for studies of molecular [4,5] and Rydberg [6] physics, to determine constraints on the variation of fundamental constants [7], for quantum simulation [8,9], and for experiments with atom arrays [10,11]. Although continuous sources of ultracold Sr atoms are under development [12,13], all these experiments operate with a duty cycle that is limited by the sample preparation time. This duty cycle fundamentally prevents optical clocks [1,14] from overcoming the standard quantum limit [15] by aliasing technical noise into the measurement results [16,17]. High repetition rates also benefit quantum simulators with ultracold atoms [18], and are a necessary requirement to implement novel schemes such as variational quantum simulation [19,20].

With this in mind, we apply the recently developed sawtooth-wave adiabatic-passage (SWAP) technique [21–24] to improve the performance of our narrow-line magneto-optical traps (MOTs), described in Sec. II. We model the cooling process using a moving three-level atom in the presence of the spatially varying magnetic field [22] in Sec. III. From this model, we conclude that the broadband cooling used in most Sr MOTs is better understood within the same adiabatic passage framework. Nevertheless, our theoretical and experimental results show that a SWAP MOT is more robust and efficient (Sec. IV). In contrast to a SWAP MOT, SWAP cooling in free space can exploit stimulated emission to cool faster than the limit imposed by the 21-μs natural lifetime of the cooling transition [23]. However, we find theoretically and experimentally that the spatially varying magnetic field of the MOT, in combination with polarization selection rules, prevents us from exploiting stimulated emission. Although a SWAP MOT does not make use of stimulated emission, it provides compelling benefits over traditional broadband laser cooling: it strongly improves the sample preparation time, efficiency, and robustness for both bosonic ^{88}Sr and fermionic ^{87}Sr isotopes.

We build on our improved understanding of the cooling process in Sec. V, where we combine three cooling stages to create 3-μK cold samples of bosonic ^{88}Sr atoms from a 1-mK cold cloud within 50 ms. These results are enabled by a novel SWAP MOT stage where only one axis is exposed to laser light at a time, but the illuminated axis is changed every 45 μs. This technique avoids unwanted stimulated processes between different axes and speeds up the SWAP cooling. In the final

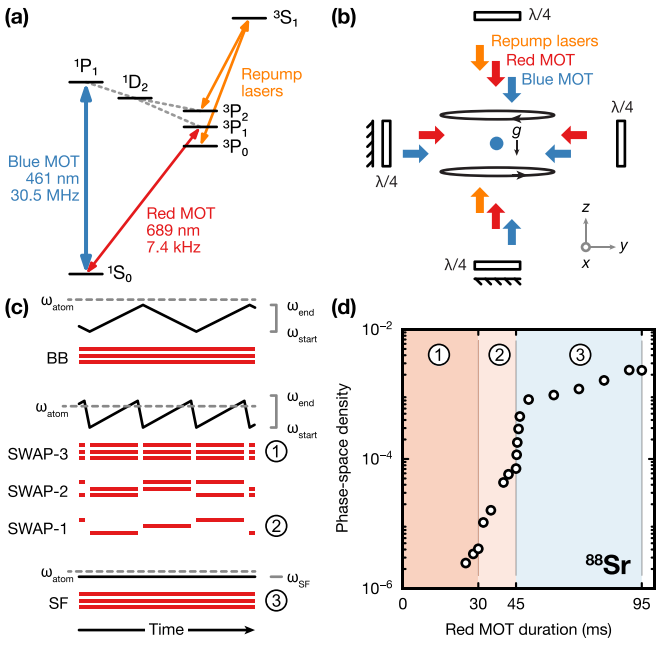

FIG. 1. (a) Strontium energy level diagram and transitions used in the experiment. We use a magneto-optical trap (blue MOT) on the $^1S_0$–$^1P_1$ transition to load a magnetic trap for the $^3P_2$ state. After repumping, we switch to a MOT on the $^1S_0$–$^3P_1$ transition (red MOT). (b) Both MOTs use retroreflected beams and the repump lasers propagate along the direction of gravity g. (c) Detuning (solid black lines) and illumination (red rectangles) sequences for the three axes used in different cooling stages of the red MOT, as explained in the text. (d) Combining sequences (1), (2), and (3) leads to high-phase-space-density ^{88}Sr samples on time scales below 100 ms.

*sebastian.blatt@mpq.mpg.de

step, we apply narrow-line laser cooling at a single frequency to reach temperatures of 1–2 μK. We also adapt our cooling method to MOTs of fermionic ^{87}Sr and demonstrate the same benefits.

II. EXPERIMENT

We load strontium atoms into a magnetic trap [25,26] for the $^3P_2$ state from a Zeeman-slowed atomic beam source. The atoms are transferred to the magnetic trap from a magneto-optical trap ("blue MOT") on the $^1S_0$–$^1P_1$ transition, with a natural linewidth $\Gamma_{\rm blue} = 2\pi \times 30.5$ MHz [see Fig. 1(a)]. The magnetic trap stores a dilute atomic gas at the Doppler temperature $T_D = \hbar\Gamma_{\rm blue}/(2k_B) = 0.7$ mK. Here, $2\pi\hbar = h$ is Planck's constant and k_B is Boltzmann's constant. For the blue MOT, we use three retroreflected laser beams at 460.86 nm with powers of (6 mW, 6 mW, 4 mW) along the (X, Y, Z) axes and $1/e^2$ waists of 6 mm, as sketched in Fig. 1(b). A pair of anti-Helmholtz coils provides the magnetic quadrupole field $B(\rho, z) = B'\sqrt{\rho^2/4 + z^2}$ for the MOT, with a gradient $B' = 63.7$ G/cm $(B'/2)$, with respect to the axial (transverse) coordinate z $(\rho = \sqrt{x^2 + y^2})$. These conditions lead to a trapped atom cloud in the linear potential, $U(\rho, z) = g(^3P_2)m(^3P_2)\mu_B B(\rho, z)$, and an exponentially decaying density profile. Here, $g(^3P_2) = 3/2$ is the magnetic g factor of the $^3P_2$ state, $m(^3P_2)$ is the magnetic quantum number, and μ_B is the Bohr magneton. The density profile for the bosonic isotope ^{88}Sr thus depends on the relative occupation of the magnetic sublevels $|m| = 1$ and 2. The density profile for the fermionic isotope ^{87}Sr is more difficult to predict, because of the hyperfine structure due to the large nuclear spin $(I = 9/2)$. The five hyperfine states have different and much smaller g factors compared to ^{88}Sr, which leads to a more extended and less tightly trapped atomic cloud. For this reason, ^{87}Sr MOTs are more susceptible to atom loss due to collisions with the atomic beam than ^{88}Sr MOTs. For our system, we find a corresponding $1/e$ magnetic trap lifetime of 24 s (16 s) for bosonic ^{88}Sr (fermionic ^{87}Sr) at an oven temperature of 600 °C. The atom number in the magnetic trap saturates when the gain by loading from the atomic beam balances this loss.

After 3 s of loading, we apply a 10-ms pulse of repumping laser light to the sample. For this purpose, we use two lasers that operate on the $^3P_2$–$^3S_1$ and $^3P_0$–$^3S_1$ transitions at 707 and 679 nm, respectively [see Fig. 1(a)]. The repump pulse transfers atoms to the $^3P_1$ state, from which they decay with a lifetime of $\tau = 21.28(3)$ μs [17] back to the $^1S_0$ ground state. For the laser intensities and magnetic fields used here, the $^1S_0$-state population is refilled with a $1/e$ time of 1.3(1) ms. In the spinless electronic ground state, the atoms experience almost no magnetic force and start to expand freely.

To further cool the atoms to the μK regime, they need to be captured in a secondary narrow-line magneto-optical trap ("red MOT") operating on the $^1S_0$–$^3P_1$ transition at $\lambda \simeq 689.4$ nm with linewidth $\Gamma = 1/\tau = 2\pi \times 7.48(1)$ kHz. For the red MOT, we use three retroreflected laser beams with $1/e^2$ waists of 3 mm and powers up to 8 mW per beam. All measurements in this paper use red light derived from a tapered amplifier, seeded with a diode laser that is itself stabilized to a high-finesse reference cavity.

The large discrepancy between red and blue transition linewidths makes it necessary to significantly broaden the linewidth of the red MOT laser to prevent atom loss: The Doppler-broadened linewidth $\Delta\omega_D = 2\pi \times \sqrt{4\hbar\Gamma_{\rm blue} \ln 2/(m\lambda^2)} \simeq 2\pi \times 0.9$ MHz is ~120 times larger than Γ. Furthermore, spatially confining atoms in a magneto-optical trap for the $^1S_0$–$^3P_1$ transition requires a magnetic quadrupole field with typical axial gradients B' of a few G/cm [25–28]. This order-of-magnitude reduction in magnetic field compared to the blue MOT has to be achieved on time scales comparable to the $^1S_0$ refilling time to prevent atoms from escaping due to their per-axis atomic root-mean-square velocity ~0.25 mm/ms. For this reason, we switch the field gradient diabatically. After the switch, we measure typical Zeeman shifts of several MHz on the red MOT transition.

The standard strategy to overcome such large Doppler and Zeeman shifts is to modulate the red MOT laser detuning at a modulation frequency $f_{\rm mod}$ over a period $t_{\rm sweep} = 1/f_{\rm mod}$. The resulting laser spectrum is a comb of frequencies spaced by $f_{\rm mod}$, and care has to be taken to find a balance between modulation speed and power-broadened linewidth. Traditionally, the resulting cooling process has been explained in terms of Doppler cooling with this modified laser spectrum. We show below that the traditional approach is more usefully described in terms of adiabatic passage processes, because optimal sweep times are comparable to the atomic lifetime τ [25–28].

We arrive at this conclusion via a thorough experimental and theoretical investigation of a novel cooling strategy, called sawtooth-wave adiabatic-passage (SWAP) cooling [21–23]. In the SWAP method, the laser frequency is ramped in a sawtooth-shaped ramp, as shown in the center panel in Fig. 1(c). Here, the laser is swept across the free-space atomic resonance to $\omega_{\rm end}$ and is rapidly reset to $\omega_{\rm start}$. This frequency sweep causes an adiabatic passage between the $^1S_0$ and the $^3P_1$ state, with an efficiency that is very insensitive to Doppler and Zeeman shifts.

Adiabatic passage is also insensitive to the direction of the frequency sweep, which requires care when resetting the laser frequency to $\omega_{\rm start}$. In our experiment, the time scale associated with changing the laser frequency is fundamentally limited by the acoustic-wave transfer time in the acousto-optical modulators that we use. To avoid another sweep across the resonance during this reset, we turn off the radio-frequency power in the acousto-optic modulators at $\omega_{\rm end}$. In combination with technical limitations in the timing system, the frequency reset results in a dark time of ~5 μs after each sweep.

Specifically, we investigated the frequency modulation and illumination sequences sketched in Fig. 1(c). In the first strategy, we use broadband-modulated laser cooling (BB), similar to traditional frequency-modulated Doppler cooling [25–28]. Here, all three MOT axes are illuminated continuously. The laser frequency is scanned in a triangle ramp between $\omega_{\rm start}$ and $\omega_{\rm end}$, such that the laser is always red-detuned from the atomic resonance at $\omega_{\rm atom}$.

As an alternative to the BB strategy, we investigated SWAP cooling in a MOT. In this method, the laser frequency is ramped in a sawtooth-shaped ramp, as shown in the center

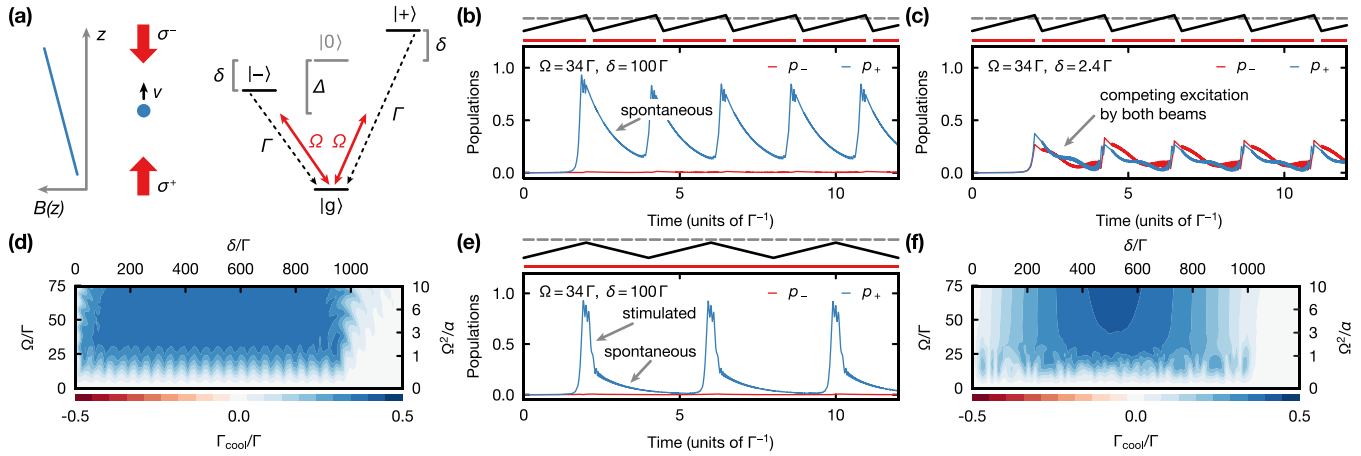

FIG. 2. (a) One-dimensional laser cooling configuration in the presence of a magnetic field gradient. We use a reduced three-level system in a V configuration to model cooling on the ^{88}Sr $^1S_0$–$^3P_1$ transition. (b) Typical population dynamics in the high-velocity (or $|\delta| \gg \Omega/\sqrt{2}$) regime. We use $t_{\text{sweep}} = 2\tau$ and $\Delta_{\text{sweep}} = 1000\,\Gamma$ for all results shown in this figure. (c) Typical population dynamics in the low-velocity (or $|\delta| \ll \Omega/\sqrt{2}$) regime where cooling stops. (d) In the adiabatic regime, where $\Omega^2/\alpha > 2/\pi$, the cooling rate Γ_{cool} is remarkably insensitive to the level splitting δ and Rabi frequency Ω. (e), (f) Traditional broadband frequency-modulated cooling can be understood within the same framework. For atoms at small $|\delta|$, the downward sweep causes stimulated emission by the *same* beam that caused the excitation on the upward sweep. This process partially cancels the desired momentum transfer, reduces the cooling rate, and causes a stronger parameter dependence in the low-$|\delta|$ regime for BB compared to SWAP.

panel in Fig. 1(c). In contrast to BB, the laser is swept across the free-space atomic resonance to ω_{end} and is rapidly reset to ω_{start}. We consider three SWAP strategies, labeled SWAP-3, SWAP-2, and SWAP-1, respectively, corresponding to the number of bright axes during each frequency sweep. Of the three, SWAP-3 is the only experimentally studied strategy so far [22].

For a given atomic cloud, any of the modulation strategies (BB, SWAP-1, SWAP-2, and SWAP-3) can be optimized to capture as many atoms as possible as quickly as possible by varying the sweep time, the start and end frequencies, the laser intensities, and the MOT beam sizes. All modulation strategies cool the atoms to the same steady-state temperature, given by the Doppler limit [23,27]. We find, however, that the strategies strongly differ in their capture efficiency and the time it takes them to reach the Doppler limit.

In this work, we demonstrate that a combination of the strategies SWAP-3 and SWAP-1 results in the highest phase-space-density samples on the shortest time scales. The SWAP-3 strategy is able to capture fast atoms at high Zeeman shifts. Once these atoms have been captured, we find that SWAP-1 becomes more efficient, because it avoids unwanted cross-axis exchange of momentum while minimizing the effects of light-assisted collisions and radiation trapping [29,30].

Regardless of the frequency modulation strategy, reducing the steady-state temperature to the few-μK regime in a strontium MOT requires a significant reduction in laser power and magnetic field gradient. Once the temperature is low enough, regular narrow-line cooling at low laser intensities without frequency modulation becomes the most efficient strategy [27]. For this reason, we add a final red-detuned single-frequency Doppler cooling step to our cooling procedure, indicated in the bottom panel in Fig. 1(c) as strategy SF.

We show typical data for the bosonic ^{88}Sr isotope in Fig. 1(d), where we gain three orders of magnitude in phase-space density in less than 100 ms. Note that most of the cooling happens within the first 50 ms of our combined sequence, which uses the SWAP-3, SWAP-1, and SF strategies consecutively. In the following section, we develop a simple model to explain both the BB strategy and the SWAP strategies within a common framework.

III. COOLING MODEL

We are interested in the average behavior of a thermal sample of three-level ^{88}Sr atoms interacting with a train of frequency-swept laser pulses on the $^1S_0$–$^3P_1$ transition in the presence of a quadrupole magnetic field. Based on our experimental results, we argue later that the population dynamics for ^{87}Sr with its 10 nuclear magnetic states can be understood in a similar framework. To model the atom-light interaction, we use a simplified model first introduced for this purpose in Ref. [22].

Specifically, we include the nondegenerate $^1S_0$ ground state $|g\rangle$ and the two stretched magnetic sublevels $|\pm\rangle$ of the $^3P_1$ state (V-type level scheme) in the optical Bloch equations for an atom moving along one dimension, say Z. Two laser beams with equal intensities and opposite circular polarizations propagate with wave vectors $\pm k\hat{z}$, where $k = 2\pi/\lambda$, as sketched in Fig. 2(a).

We treat the atomic position z and velocity v classically and thus can combine the Doppler and Zeeman shifts of $|\pm\rangle$ into a single parameter, $\delta = kv + g(^3P_1)m(^3P_1)\mu_B B' z/\hbar$, that describes the energy splitting between the states $|\pm\rangle$ corresponding to the magnetic quantum numbers $m(^3P_1) = \pm 1$. The $J = 0 \to J = 1$ transition under consideration leads to equal Clebsch-Gordan factors of $1/\sqrt{3}$ for all possible transitions. Although we use retroreflected laser beams, which produce a standing wave with rotating linear polarization at each position, $|\delta| > 0$ locally selects the resonant transition

and the cooling process terminates as soon as $|\delta|$ locally becomes small compared to the power-broadened linewidth. For a magnetic quadrupole field, the atom is thus cooled to a drift velocity pointing towards the magnetic field zero.

The above considerations result in an equal Rabi frequency, $\Omega \equiv \Gamma/\sqrt{3}\sqrt{s_0/2}$, for each beam. Here, $s_0 = I_{\rm pk}/I_{\rm sat}$ is the saturation parameter in terms of the saturation intensity $I_{\rm sat} = \pi hc/(3\lambda^3\tau)$ and the Gaussian laser beams' peak intensity $I_{\rm pk} = 2P/(\pi w_0^2)$, with beam power P and $1/e^2$ waist w_0, respectively. We also allow for the lasers to be switched off by letting $\Omega(t)$ vary with time. The laser frequency for each beam is scanned simultaneously as $\Delta(t) \equiv \Delta_0 + 2\pi f(t)$, starting at a fixed initial detuning $\Delta_0 \equiv \omega_{\rm start} - \omega_{\rm atom}$ and continuing with a periodic frequency ramp $f(t)$.

Under these assumptions, we find the time-dependent Hamiltonian

$$H(t)/\hbar = \begin{pmatrix} \Delta(t)+\delta & 0 & \Omega(t)/2 \\ 0 & \Delta(t)-\delta & \Omega(t)/2 \\ \Omega^*(t)/2 & \Omega^*(t)/2 & 0 \end{pmatrix} \tag{1}$$

and the optical Bloch equations for the density matrix ρ

$$\dot{\rho} = -i[H(t)/\hbar, \rho] + \mathcal{L}\rho. \tag{2}$$

We model the effects of spontaneous emission on the elements of the density matrix by the Liouvillian

$$\mathcal{L}\rho = -\Gamma \begin{pmatrix} \rho_{11} & \rho_{12} & \rho_{13}/2 \\ \rho_{21} & \rho_{22} & \rho_{23}/2 \\ \rho_{31}/2 & \rho_{32}/2 & -\rho_{11}-\rho_{22} \end{pmatrix}. \tag{3}$$

This model is useful to describe the loading and initial cooling of the red MOT because the atomic velocity and position do not change significantly on the time scale of the cycle time $t_{\rm cycle} \equiv t_{\rm sweep} + t_{\rm dark}$, which in all cases of interest is of the order of the atomic lifetime τ. This condition places the initial stage of frequency-swept laser cooling in the red MOT in an interesting regime. We work neither in the adiabatic rapid passage regime, where $t_{\rm cycle} \ll \tau$, nor fully in the steady state with respect to atomic decay, where $t_{\rm cycle} \gg \tau$. For this reason, adiabatic approximations of the Bloch equations produce misleading results and we have to rely on numerical solutions to explain our experimental results. For instance, we show the population dynamics of a typical pulse train for a representative sweep (dead) time of $t_{\rm sweep} = 2\tau$ ($t_{\rm dead} = 0.238\tau$) in the high-velocity regime in Fig. 2(b). Here, an atom at detuning $\delta = 100\,\Gamma$ is exposed to a train of laser pulses whose frequency is swept over $\Delta_{\rm sweep} = 1000\,\Gamma$, ending at $\omega_{\rm end} - \omega_{\rm atom} = +13.3\,\Gamma$, with a Rabi frequency of $\Omega = 34\,\Gamma$. Because of the large splitting between the excited states, the pulse train efficiently excites only the $|+\rangle$ state. After the first excitation, spontaneous emission reinitializes the atom to a ground-state fraction depending on $t_{\rm cycle}/\tau$. We find that the population dynamics reliably settle to a periodic pattern for all parameter ranges in this work after a few cycles.

Even though we have to use numerics, we can identify useful analytic expressions for some of the parameters, such as the condition for adiabatic passage, if spontaneous emission is neglected. Assuming that Ω is constant and that the detuning is ramped across the resonance with constant frequency slope $\alpha \equiv 2\pi\dot{f} = \Delta_{\rm sweep}/t_{\rm sweep}$, the Landau-Zener probability for adiabatic passage to the excited state [23],

$$p_{\rm LZ} = 1 - \exp\left(-\frac{\pi}{2}\frac{\Omega^2}{\alpha}\right), \tag{4}$$

is only determined by the adiabaticity parameter Ω^2/α. Note again that this result requires $t_{\rm cycle} \ll \tau$ but that it will be useful to benchmark our experimental and numerical results. In particular, the excited-state population never reaches $p_{\rm LZ}$, because it decays during the whole excitation process.

We can also see from Eq. (1) that if $|\delta| \ll \Omega/\sqrt{2}$, because the velocity and the Zeeman splitting are small or compensate each other, we have a competition between adiabatic passage from the ground state to either of the excited states $|\pm\rangle$. If there is no imbalance between the transition probabilities to $|\pm\rangle$, the cooling efficiency vanishes, because the atom absorbs a photon from each of the counterpropagating beams. Typical population dynamics for $\delta = 2.4\,\Gamma$ are shown in Fig. 2(c).

The transition from cooling to heating leads to a balance where one finds the same steady-state temperature $k_B T_{\rm ss} = \hbar\Omega/2$ as for Doppler cooling as long as one cannot take advantage of stimulated processes where the atom is stimulated back to the ground state by the *other* beam [23]. In contrast to SWAP cooling in free space [21], it is not possible to realize this situation in a SWAP MOT [22], because opposite circular polarizations are used in combination with a magnetic field gradient to create localization. In a situation where one can separate atomic localization from the excitation process, such as in a magic-wavelength optical dipole trap, SWAP cooling could be much more effective with the exploitation of stimulated emission in the regime of $t_{\rm cycle} \ll \tau$ as originally envisioned [21,23].

To describe the efficiency of the cooling process, we introduce the laser cooling rate

$$\Gamma_{\rm cool} \equiv \Gamma\,\mathrm{sign}(\delta)\langle p_+ - p_-\rangle_{\rm cycle} \tag{5}$$

as the difference between the scattering rates due to the cycle-averaged probabilities of exciting the corresponding states $p_+ \equiv \rho_{11}$ and $p_- \equiv \rho_{22}$, respectively. Because the SWAP cooling process is based on adiabatic passage, this cooling rate is remarkably insensitive to laser frequency or intensity drifts, as shown in Fig. 2(d).

Interestingly, we can understand the broadband-modulated laser cooling, traditionally used in narrow-line magneto-optical traps for Sr [25–27], within the same framework: In Fig. 2(e), we show population dynamics for a pulse train where the laser frequency is ramped in a triangle pattern with the same slope (Rabi frequency) α (Ω) as in Figs. 2(b) and 2(c), such that the adiabaticity parameter remains the same. The laser is never turned off ($t_{\rm dead} = 0$) and the detuning ramp still spans $\Delta_{\rm sweep} = 1000\,\Gamma$ but ends to the red of the resonance at $\omega_{\rm end} - \omega_{\rm atom} = -13.3\,\Gamma$. We immediately see the disadvantage of this BB strategy compared to the SWAP-1 strategy, in that p_+ is not allowed to decay spontaneously but is stimulated back to the ground state on the downslope of the ramp by the *same* beam that excited it. This stimulated process produces a momentum kick opposite to the initial excitation, reduces the amount of spontaneous scattering, and thus reduces $\Gamma_{\rm cool}$.

As shown in Fig. 2(f), the BB strategy works well when the time between adiabatic transfers on the up- and downslope of the frequency ramp is long enough for a significant fraction of p_+ to decay, because adiabatic passage is insensitive to the direction of the frequency sweep across the resonance. However, the cooling efficiency is strongly reduced for low-$|\delta|$ atoms compared to SWAP-1. Some of this efficiency can be recovered by modulating the laser frequency in a sinusoidal fashion (reduced α at small $|\delta|$) as traditionally done [27,28], but SWAP is more efficient.

In conclusion, we find that the adiabatic passage picture provides a better framework to understand both traditional BB and SWAP cooling strategies. In addition, the model predicts that, compared to BB, SWAP has three advantages. First, it optimizes the excitation process for low-velocity atoms at low Zeeman shifts. Second, it makes the cooling process more homogeneous across the whole thermal sample loaded from the magnetic trap. Finally, it is more robust with respect to intensity fluctuations.

In the subsequent section, we show experimental results that support this conclusion and discuss secondary experimental conditions that influence the choice of cooling strategy.

IV. SWAP MOT

Before discussing the full cooling sequence shown in Fig. 1(d), we demonstrate the strengths and weaknesses of the SWAP and BB cooling strategies experimentally by keeping the magnetic field and laser intensity constant. Based on our results, we design magnetic field and intensity ramps to increase the phase-space density as quickly as possible without losing atoms. With these ramps, we find that SWAP-3 has a high capture efficiency while cooling more rapidly than BB. Once high-velocity atoms at high Zeeman shifts are captured, we find it advantageous to switch to SWAP-1, because of its faster cooling speed at low temperatures. We demonstrate a combined strategy that exploits the advantages of SWAP-3 and SWAP-1. By varying its parameters, we show that we can understand the cooling of both bosonic ^{88}Sr and fermionic ^{87}Sr isotopes within the adiabatic passage framework of Sec. III.

A. Cooling at constant intensity and constant magnetic field

In the first experiment, we cool the atoms for a duration $t_{\rm red}$ while keeping the magnetic field gradient and the laser power constant. In Fig. 3(a), we show how the peak density of the resulting MOT evolves with $t_{\rm red}$ for the BB, SWAP-1, and SWAP-3 strategies. All cooling strategies use a magnetic field gradient of $B' = 3$ G/cm, a red laser power of 2 mW per axis, and a sweep range of ∼11 MHz. The SWAP strategies end at a (blue) detuning of 100 kHz, while the BB strategy ends at a (red) detuning of −100 kHz. We use a sweep time $t_{\rm sweep} = 40$ μs (80 μs) for SWAP (BB).

Compared to the SWAP strategies, BB exhibits a lower initial density but a slower decay at long times. We determine both the $1/e$-lifetime $\tau_{\rm MOT}$ and the two-body-loss rate coefficient K_2 for all strategies by fitting the solution of $\dot{n} = -n/\tau_{\rm MOT} - K_2 n^2$ to the density data in Fig. 3(a). We find that the red-detuned BB strategy leads to a MOT with $\tau_{\rm MOT} =$

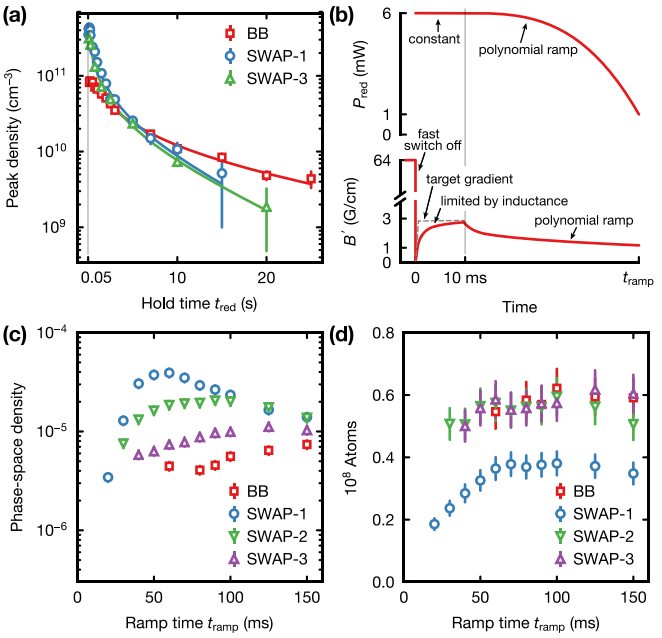

FIG. 3. (a) The peak density decreases as a function of the hold time when the intensity and magnetic field gradient are held constant. At short times, light-assisted collisions at high densities lead to loss for all cooling strategies. (b) Optimized ramp of the light intensity and magnetic field gradient used to measure phase-space densities (c) and atom numbers (d) versus ramp time $t_{\rm ramp}$ for all modulation strategies.

25 ± 10 s, comparable to the lifetime of atoms in the magnetic trap. We thus attribute this one-body loss to collisions with the atomic beam. The SWAP-1 and SWAP-3 strategies lead to a reduced $\tau_{\rm MOT} = 7(2)$ and 8(2) s, respectively. In addition, all strategies show nonexponential loss at short times, due to light-assisted scattering on the repulsive V_{1u} asymptote [31]. We find similar two-body-loss rate coefficients $K_2 \simeq 5(1) \times 10^{-12}$ cm^3/s for all strategies at this laser power.

Note that the plotted initial peak density differs between cooling strategies because irregular density profiles for $t_{\rm red} \lesssim 50$ ms prevent us from reliably measuring the in-trap density profile with absorption imaging. To image the atoms, we turn off the magnetic field gradient and the laser beams at the end of $t_{\rm red}$ and either image the atoms immediately (*in situ*) or allow the atoms to fall for 15 ms before imaging. We take two absorption images on the $^1S_0$–$^1P_1$ transition simultaneously by exposing the atomic cloud for 50 μs to two separate probe beams propagating along Y and Z, respectively. The probe beams have a resonant saturation parameter of ∼0.1 to avoid having to compensate for saturated absorption in the sample, while the exposure time minimizes position and size changes of the cloud [32]. For optical densities above ∼2, we detune the probe beams to ensure that we use the dynamic range of our cameras optimally. Using standard methods, we extract the temperature, atom number, and in-trap phase-space density of the atomic cloud. The error bars for these quantities combine a 10% shot-to-shot atom number fluctuation with the statistical fit error.

From these measurements, we conclude that we need to optimize the capture fraction from the magnetic trap, while

minimizing the losses due to light-assisted collisions. Although all strategies show the same two-body loss, the SWAP strategies lead to four times higher densities on short time scales than BB. To make use of SWAP's improved cooling speed, we thus need to find a balance between density and temperature.

B. Optimized intensity and magnetic field ramps

Previous attempts at optimizing the broadband stage of the red MOT made a choice between quickly cooling only the coldest atoms for atomic clocks [27] and slowly cooling almost all atoms for quantum gas experiments [26]. Armed with our understanding of the SWAP strategies, we dynamically changed the laser power per beam P_{red} and the magnetic field gradient B' to obtain the coldest samples in the shortest times. The steady-state temperature of all cooling strategies is proportional to the laser intensity, and the shape of the atomic cloud is determined by the magnetic field gradient [27]. Since the atoms transferred from the magnetic trap are dilute and hot initially, we initially operate the red MOT at a high gradient and beam power to capture as many atoms as possible. Following the fast switch-off of the magnetic field gradient for the blue MOT, we set the current to an empirically optimized gradient, $B' = 3$ G/cm, as shown in Fig. 3(b). Our system takes ∼10 ms to reach the desired gradient after the switch-off, limited by the coil inductance. During this time, we keep the red laser power constant at $P_{\mathrm{red}} = 6$ mW. To reduce the steady-state temperature and the density, we then ramp down both B' and P_{red} using the empirically optimized polynomial ramps shown in Fig. 3(b). We find that the different strategies produce samples with dramatically different phase-space densities as a function of the total ramp time.

In Fig. 3(c), we see that all strategies have an optimal associated time: If we ramp too quickly, the phase-space density remains low. If we ramp too slowly, we start to lose phase-space density due to light-assisted collisions between the coldest atoms. We also see that SWAP-1 produces the highest phase-space densities, while BB performs the worst. The SWAP-1 strategy achieves this goal despite losing 40% of the atoms, as shown in Fig. 3(d). This loss is not present in the other strategies, and we attribute this loss to hot atoms that escape from the cooling region while the corresponding axes are not illuminated.

C. Combining SWAP-3 with SWAP-1

Based on these results, we decided to combine the high capture efficiency of SWAP-3 with the fast and efficient cooling of SWAP-1. We use the same laser power and magnetic field ramps as in Fig. 3(b) but switch from SWAP-3 to SWAP-1 at a time $t_{\mathrm{switch}} < t_{\mathrm{ramp}}$. We optimized t_{switch} and the SWAP cooling parameters of this combined sequence in detail for both bosonic ^{88}Sr and fermionic ^{87}Sr isotopes and found that its performance is limited by the initial capture fraction of SWAP-3 from the magnetic trap.

In Fig. 4(a), we show the atom number at $t_{\mathrm{ramp}} = 45$ ms (150 ms) for ^{88}Sr (^{87}Sr) versus the initial power per beam P_{init}. We trap 1.5×10^8 ^{88}Sr (1.0×10^7 ^{87}Sr) atoms for $P_{\mathrm{init}} = 8$ mW. The data suggest that we reach the adiabatic

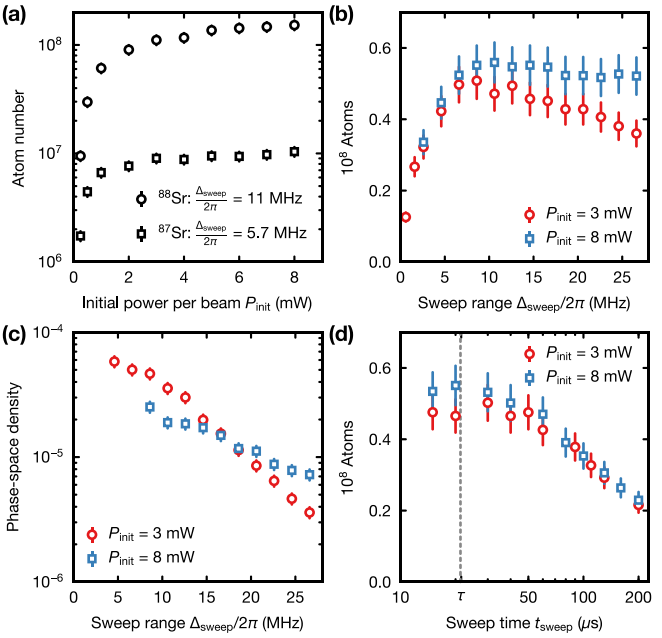

FIG. 4. (a) The atom number in the SWAP MOT for an 8.5-MHz sweep range saturates as a function of the initial laser power per beam P_{init} for ^{88}Sr and ^{87}Sr. (b) For ^{88}Sr, the atom number saturates for high powers per beam (blue squares) as a function of the sweep range but decreases linearly for large sweep ranges at low powers (red circles). (c) At the same time, the phase-space density decreases exponentially. (d) Longer sweep times preclude capturing the fastest atoms from the magnetic trap. Sweep times shorter than the natural lifetime τ do not increase the capture fraction further.

passage regime for relatively low initial powers. We find that a sweep range of $\Delta_{\mathrm{sweep}} = 2\pi \times 11$ MHz ($2\pi \times 5.7$ MHz) for ^{88}Sr (^{87}Sr) produces a comparable power dependence for both isotopes. The ratio between sweep ranges is consistent with similar cooling conditions requiring similar adiabaticity parameters and the lower average scattering rate for the $F = 9/2 \rightarrow F' = 11/2$ transition in ^{87}Sr compared to the $J = 0 \rightarrow J' = 1$ transition in ^{88}Sr. The final number of ^{87}Sr atoms is ∼80% of the value suggested by the relative natural abundance of ^{87}Sr and ^{88}Sr (7.00% and 82.58%). We attribute this discrepancy to the more extended atomic density profile in the magnetic trap (see Sec. II). If sufficient optical power is available, increasing the beam sizes could lead to an improved capture fraction. For a given beam size, the capture fraction of the SWAP MOT seems to be proportional to the adiabaticity parameter if we take into account that ^{87}Sr scatters less cooling light than ^{88}Sr.

In the remainder of Fig. 4, we explore the SWAP cooling parameters for two representative initial powers: (i) a "low" power per beam of 3 mW, which is available from a typical diode laser at 689 nm; and (ii) a "high" power per beam of 8 mW, which requires multiple diode lasers or a tapered amplifier. For brevity, we only show data for ^{88}Sr, because we find equivalent results for ^{87}Sr, with the caveat of a reduced scattering rate that requires a reduced sweep range for the same power.

When we vary the sweep range Δ_{sweep} by varying ω_{start}, we find the data shown in Fig. 4(b). For high power, the atom

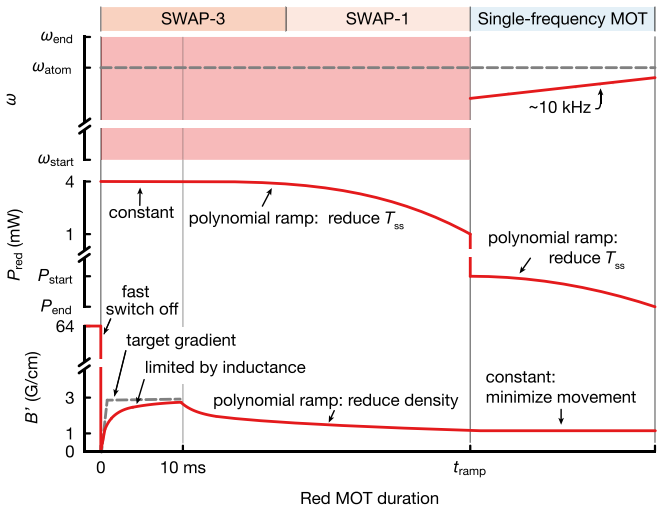

FIG. 5. Optimized experimental sequence used for both ^{88}Sr and ^{87}Sr magneto-optical traps. The cooling technique in a given interval is indicated at the top (SWAP-3, SWAP-1, or single-frequency MOT). Top, middle, and bottom graphs show the red MOT beam frequency spectrum, power, and gradient traces versus the red MOT duration, respectively.

number first increases and then saturates because an increased sweep range can address atoms at higher Zeeman shifts. For low power, the atom number peaks but then slowly decreases with the linear decrease in the adiabaticity parameter. Even though the atom number shows a similar behavior in the low- and high-power limits, the phase-space density decreases exponentially with an increased sweep range, as shown in Fig. 4(c). This behavior is consistent with an exponential decrease in the cooling rate due to the reduced adiabatic transfer efficiency $\propto p_{LZ}$. We show in Fig. 4(d) that the sweep time influences the number of atoms dramatically as well: the cooling rate is too low to capture the fastest atoms for increased sweep times. Finally, we find that reducing the sweep time below the natural lifetime does not improve the number of captured atoms in the SWAP MOT, consistent with the predictions of the optical Bloch equations in Sec. III.

V. SINGLE-FREQUENCY MOT

As the last step in our cooling protocol, we use traditional narrow-line laser cooling at a single frequency to reach final temperatures of 1–2 μK. We start the red MOT with the optimized SWAP combination sequence discussed in Sec. IV. The laser frequency is scanned from $\omega_{start} - \omega_{atom} = -2\pi \times 8.5$ MHz (-4.2 MHz) to $\omega_{end} - \omega_{atom} = 2\pi \times 0.1$ MHz for ^{88}Sr (^{87}Sr) as shown in the upper panel in Fig. 5. At the same time, the laser power and magnetic field gradient are slowly ramped with the polynomial shapes shown in Fig. 5. After reaching the steady state of the combined technique, we switch to the single-frequency MOT at t_{ramp} to further cool the sample. To switch to the SF strategy, we select cooling parameters that would leave the cloud shape and temperature unchanged. Thus, we turn off the frequency scan, set the laser frequency to a -80-kHz (-10-kHz) red detuning, and quickly lower the beam power from 1 mW to $P_{start} = 35\ \mu W$ (20 μW) for ^{88}Sr (^{87}Sr). Finally, we ramp the beam power once again with a polynomial shape to $P_{end} = 1\ \mu W$ (0.5 μW) for ^{88}Sr (^{87}Sr) to reduce the steady-state temperature of the cooling process. To ensure fast cooling during the single-frequency MOT, we minimize the atomic movement along gravity caused by the change in the detuning and gradient [27]. We thus limit the detuning ramp amplitude to only ~10 kHz and keep the gradient constant.

The series of *in situ* absorption images of ^{88}Sr in Fig. 6(a) illustrates the cooling process. The SWAP-3 strategy allows us to capture about 9×10^7 atoms, but the cloud remains large and dilute. As soon as we switch to SWAP-1, the atomic cloud shrinks visibly. In the single-frequency MOT, the atoms sag along the direction of gravity while cooling to a few μK, which is a characteristic behavior of the bosonic narrow-line MOT [27]. We cool to 3 μK after 5 ms of the single-frequency MOT without losing atoms. The phase-space density at this point is 8×10^{-4}, a factor of 400 larger than for the case of a red MOT time of 25 ms (prior to this, we cannot get reliable estimates due to irregular *in situ* shapes). The phase-space density increases further over the final 45 ms of single-frequency cooling and reaches 2×10^{-3} at a final temperature of 2 μK, at the expense of losing 25% of the atoms. Note that this final cooling step in the single-frequency MOT takes the

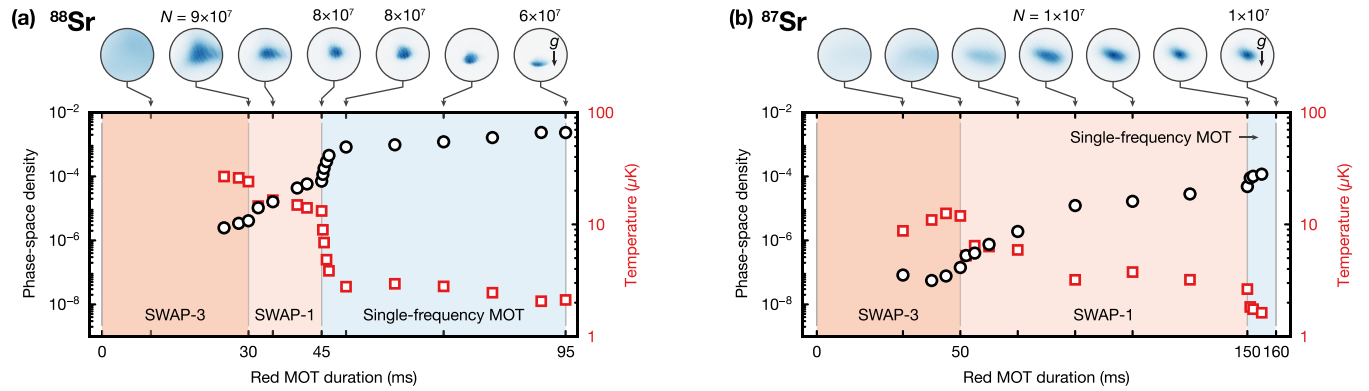

FIG. 6. (a) Measured temperatures (red squares) and phase-space densities (black circles) versus red MOT duration for ^{88}Sr. The label at the bottom (SWAP-3, SWAP-1, or single-frequency MOT) specifies the active cooling strategy. *In situ* images taken at different red MOT times are shown at the top with the atom number (N) and the direction of gravity (g). (b) We find comparable results for ^{87}Sr when taking the reduced scattering rate into account.

same amount of time as the entire initial cooling procedure, pointing towards a mechanism that competes with the cooling process while the ^{88}Sr atoms sag to the lower edge of the MOT. This atom loss is likely due to a combination of light-assisted collisions and radiation trapping [29,30].

We apply the same protocol to ^{87}Sr but increase its cooling efficiency by adding red stirring laser beams [25], which copropagate with the red MOT beams. The *in situ* images in Fig. 6(b) show the cooling progress for ^{87}Sr. Unlike ^{88}Sr, with its vanishingly small scattering length, the ^{87}Sr sample does not sag under gravity. Instead, it thermalizes by interparticle collisions [25,26]. We observe larger and more dilute initial atomic clouds of ^{87}Sr than of ^{88}Sr during SWAP-3, because of the reduced cooling rate discussed in the previous section. For the same reason, it takes longer to cool the ^{87}Sr cloud to the steady state in the subsequent SWAP-1 cooling stage. In total, we find that we need to operate the SWAP MOT about three times longer for ^{87}Sr than for ^{88}Sr. We reach a temperature of 3 μK and a phase-space density of 5×10^{-5} at the end of SWAP-1. The subsequent 10 ms of single-frequency MOT cools the atoms further, reaching a final temperature of 1.4 μK and a phase-space density of 1.4×10^{-4} without atom loss.

VI. CONCLUSION

We have demonstrated a new method to create high-phase-space-density samples in a narrow-line magneto-optical trap (MOT) using sawtooth-wave adiabatic-passage (SWAP) cooling. With a simple model, we have shown that even the traditional broadband-modulated laser cooling used in most Sr MOTs is better understood within the adiabatic passage framework. Our theoretical studies predict and our experimental results show that a SWAP MOT is more robust and efficient than the traditional broadband-modulated MOT.

We investigated three SWAP MOT strategies. We found that illuminating all axes in the SWAP-3 strategy leads to the largest capture fraction from the magnetic trap. Once the atoms have been captured and cooled to the steady-state temperature, it is beneficial to illuminate only one MOT axis at a time. This SWAP-1 strategy reduces light-assisted collisions, avoids unwanted stimulated exchange of momentum between different axes, and thus leads to a much faster cooling speed at low temperatures. At very low temperatures, regular narrow-line Doppler cooling at a single frequency becomes the optimal strategy (SF). To exploit the advantages of SWAP-3, SWAP-1, and SF, we combined them in an optimal way. With this combined sequence, we created high-phase-space-density samples of bosonic ^{88}Sr and fermionic ^{87}Sr atoms within 50 and 160 ms, respectively. Our results for ^{88}Sr also suggest that the narrow-line, single-frequency cooling stage produces most of its effect on time scales of 10 ms before it becomes limited by density-dependent effects [29,30].

Our method is simple to implement, and in combination with high-flux atomic sources [30,33,34], it can be used to improve the duty cycle of atomic clocks and the repetition rate of precision experiments and quantum simulations. Extending our method by a final dark-spot MOT stage [35] might result in even lower final temperatures and higher phase-space densities. We expect that our cooling method can also benefit narrow-line magneto-optical traps for other two-electron atoms, lanthanides, and molecules.

ACKNOWLEDGMENTS

We thank N. Janša, R. González Escudero, S. Wissenberg, F. Finger, R. Haindl, E. Staub, A. Mayer, and K. Förster for technical contributions to the construction of the experiment and N. Šantić for critical reading of the manuscript. This work was supported by funding from the UQUAM ERC Synergy Grant. A.J.P. was supported by a fellowship from the Natural Sciences and Engineering Research Council of Canada (NSERC), funding ref. no. 517029.

[1] A. D. Ludlow, M. M. Boyd, J. Ye, E. Peik, and P. O. Schmidt, Rev. Mod. Phys. **87**, 637 (2015).

[2] M. A. Norcia, J. R. K. Cline, J. A. Muniz, J. M. Robinson, R. B. Hutson, A. Goban, G. E. Marti, J. Ye, and J. K. Thompson, Phys. Rev. X **8**, 021036 (2018).

[3] L. Hu, N. Poli, L. Salvi, and G. M. Tino, Phys. Rev. Lett. **119**, 263601 (2017).

[4] V. Barbé, A. Ciamei, B. Pasquiou, L. Reichsöllner, F. Schreck, P. S. Żuchowski, and J. M. Hutson, Nat. Phys. **14**, 881 (2018).

[5] S. S. Kondov, C.-H. Lee, M. McDonald, B. H. McGuyer, I. Majewska, R. Moszynski, and T. Zelevinsky, Phys. Rev. Lett. **121**, 143401 (2018).

[6] R. Ding, J. D. Whalen, S. K. Kanungo, T. C. Killian, F. B. Dunning, S. Yoshida, and J. Burgdörfer, Phys. Rev. A **98**, 042505 (2018).

[7] S. Blatt, A. D. Ludlow, G. K. Campbell, J. W. Thomsen, T. Zelevinsky, M. M. Boyd, J. Ye, X. Baillard, M. Fouché, R. Le Targat, A. Brusch, P. Lemonde, M. Takamoto, F.-L. Hong, H. Katori, and V. V. Flambaum, Phys. Rev. Lett. **100**, 140801 (2008).

[8] S. Kolkowitz, S. L. Bromley, T. Bothwell, M. L. Wall, G. E. Marti, A. P. Koller, X. Zhang, A. M. Rey, and J. Ye, Nature **542**, 66 (2016).

[9] S. V. Rajagopal, K. M. Fujiwara, R. Senaratne, K. Singh, Z. A. Geiger, and D. M. Weld, Ann. Phys. **529**, 1700008 (2017).

[10] A. Cooper, J. P. Covey, I. S. Madjarov, S. G. Porsev, M. S. Safronova, and M. Endres, Phys. Rev. X **8**, 041055 (2018).

[11] M. A. Norcia, A. W. Young, and A. M. Kaufman, Phys. Rev. X **8**, 041054 (2018).

[12] S. Bennetts, C.-C. Chen, B. Pasquiou, and F. Schreck, Phys. Rev. Lett. **119**, 223202 (2017).

[13] C.-C. Chen, S. Bennetts, R. G. Escudero, F. Schreck, and B. Pasquiou, arXiv:1810.07157.

[14] W. M. Itano, J. C. Bergquist, J. J. Bollinger, J. M. Gilligan, D. J. Heinzen, F. L. Moore, M. G. Raizen, and D. J. Wineland, Phys. Rev. A **47**, 3554 (1993).

[15] V. B. Braginsky and F. Y. Khalili, in *Quantum Measurement*, edited by K. S. Thorne (Cambridge University Press, Cambridge, UK, 1992).

[16] G. Santarelli, C. Audoin, A. Makdissi, P. Laurent, G. Dick, and A. Clairon, IEEE Trans. Ultrason. Ferroelectr. Freq. Control **45**, 887 (1998).

[17] T. Nicholson, S. Campbell, R. Hutson, G. Marti, B. Bloom, R. McNally, W. Zhang, M. Barrett, M. Safronova, G. Strouse, W. Tew, and J. Ye, Nat. Commun. **6**, 6896 (2015).

[18] I. Bloch, J. Dalibard, and S. Nascimbène, Nat. Phys. **8**, 267 (2012).

[19] B. P. Lanyon, J. D. Whitfield, G. G. Gillett, M. E. Goggin, M. P. Almeida, I. Kassal, J. D. Biamonte, M. Mohseni, B. J. Powell, M. Barbieri, A. Aspuru-Guzik, and A. G. White, Nat. Chem. **2**, 106 (2010).

[20] C. Kokail, C. Maier, R. van Bijnen, T. Brydges, M. K. Joshi, P. Jurcevic, C. A. Muschik, P. Silvi, R. Blatt, C. F. Roos, and P. Zoller, Nature **569**, 355 (2019).

[21] M. A. Norcia, J. R. K. Cline, J. P. Bartolotta, M. J. Holland, and J. K. Thompson, New J. Phys. **20**, 023021 (2018).

[22] J. A. Muniz, M. A. Norcia, J. R. K. Cline, and J. K. Thompson, arXiv:1806.00838.

[23] J. P. Bartolotta, M. A. Norcia, J. R. K. Cline, J. K. Thompson, and M. J. Holland, Phys. Rev. A **98**, 023404 (2018).

[24] N. Petersen, F. Mühlbauer, L. Bougas, A. Sharma, D. Budker, and P. Windpassinger, arXiv:1809.06423.

[25] T. Mukaiyama, H. Katori, T. Ido, Y. Li, and M. Kuwata-Gonokami, Phys. Rev. Lett. **90**, 113002 (2003).

[26] S. Stellmer, R. Grimm, and F. Schreck, Phys. Rev. A **87**, 013611 (2013).

[27] T. H. Loftus, T. Ido, M. M. Boyd, A. D. Ludlow, and J. Ye, Phys. Rev. A **70**, 063413 (2004).

[28] T. Chanelière, L. He, R. Kaiser, and D. Wilkowski, Eur. Phys. J. D **46**, 507 (2008).

[29] H. Katori, T. Ido, Y. Isoya, and M. Kuwata-Gonokami, Phys. Rev. Lett. **82**, 1116 (1999).

[30] T. Yang, K. Pandey, M. S. Pramod, F. Leroux, C. C. Kwong, E. Hajiyev, Z. Y. Chia, B. Fang, and D. Wilkowski, Eur. Phys. J. D **69**, 226 (2015).

[31] T. Zelevinsky, M. M. Boyd, A. D. Ludlow, T. Ido, J. Ye, R. Ciuryło, P. Naidon, and P. S. Julienne, Phys. Rev. Lett. **96**, 203201 (2006).

[32] S. Blatt, Ph.D. thesis, University of Colorado, 2011.

[33] S. B. Nagel, P. G. Mickelson, A. D. Saenz, Y. N. Martinez, Y. C. Chen, T. C. Killian, P. Pellegrini, and R. Côté, Phys. Rev. Lett. **94**, 083004 (2005).

[34] P. G. Mickelson, Y. N. Martinez, A. D. Saenz, S. B. Nagel, Y. C. Chen, T. C. Killian, P. Pellegrini, and R. Côté, Phys. Rev. Lett. **95**, 223002 (2005).

[35] S. Stellmer, B. Pasquiou, R. Grimm, and F. Schreck, Phys. Rev. Lett. **110**, 263003 (2013).